

# Effect of Sb doping on the structural, electrical, and optical properties of SnO<sub>2</sub> thin films prepared through spray pyrolysis

M. R. Fadavieslam<sup>1</sup>

Received: 16 November 2015 / Accepted: 18 January 2016 / Published online: 27 January 2016  
© Springer Science+Business Media New York 2016

**Abstract** In this research, antimony-doped tin dioxide (ATO) films were deposited on glass substrates at  $T = 550$  °C through spray pyrolysis. The effects of antimony doping on the structural, optical, and electrical properties of the thin films were investigated. Tin chloride ( $\text{SnCl}_4 \cdot 5\text{H}_2\text{O}$ ) and antimony chloride ( $\text{SbCl}_3$ ) were used as a host and a dopant precursor, respectively. X-ray diffraction (XRD) analysis indicated that the undoped SnO<sub>2</sub> thin film exhibited a preferred (211) orientation. As the Sb doping concentration increased, a different preferred (200) orientation was observed. Field emission scanning electron microscopy analysis revealed polyhedron-like grains of the thin films. Atomic force microscopy analysis demonstrated that the minimum and maximum amounts of roughness were within the  $\frac{[\text{Sb}]}{[\text{Sn}]}$  % molar ratio of 10 and 7.5 at.% concentrations, respectively. As the doping concentration increased, the average grain size initially increased and then decreased; electrical resistance initially decreased and subsequently increased; the carrier concentration and Hall mobility initially increased and then decreased; and Seebeck coefficient decreased. The optical band gap of the thin films ranged from 3.16 to 3.8 eV. Hall effect and thermoelectric studies revealed that the films exhibited an n-type conductivity.

## 1 Introduction

Transparent conducting oxide (TCO) films, such as SnO<sub>2</sub>, In<sub>2</sub>O<sub>3</sub>, and ZnO, are widely used in various optoelectronic devices, such as solar cells, displays, and electrochromic devices [1–9]. SnO<sub>2</sub> is a traditional, low-cost, and multi-functional material, which can be used as a gas sensor, oxide catalyst, and transparent conductor because of its oxygen vacancy and dual valence [10–13]. Tin dioxide (SnO<sub>2</sub>) films have been extensively investigated because of their wide range of applications in industry and research [14]. SnO<sub>2</sub> is a wide-band-gap (3.6–3.8 eV) semiconductor that exhibits an n-type conductivity without intentional doping [11, 15–19]. This semiconductor is extensively used in various applications, including solar energy conversion, catalysis, gas sensing, antistatic coating, transparent electrode, varistors, optoelectronic devices and display panels [17, 19, 20]. However, stoichiometric SnO<sub>2</sub> exhibits low optical and electrical performance because of its low intrinsic carrier density and mobility [14]. It is a technologically important material because of its various applications, such as gas sensors, chemical sensors, and transparent conducting thin films. For most SnO<sub>2</sub> applications, impurities should be doped to modify its conductivity, optical absorption, and gas sensitivity [11]. Doped SnO<sub>2</sub> thin films have been widely used as transparent electrodes in various substances, such as solar cells, optoelectronic devices, flat panel displays, heat mirrors, and gas sensors, because of their high electrical conductivity and high optical transmittance in visible light and high infrared reflectance [21]. Fluorine (F), indium (In), and antimony (Sb) have also been used in doping to improve the optical properties and conductivity of SnO<sub>2</sub> [16, 22, 23]. Among these substances, Sb is the most effective and least costly; as such, Sb has been considered

✉ M. R. Fadavieslam  
m.r.fadavieslam@du.ac.ir

<sup>1</sup> School of Physics, Damghan University, Damghan, Iran

as a potential material of low-emission glass [14]. SnO<sub>2</sub>:Sb (ATO) is a common transparent conductive material [10]. Previous studies focused on the optical and electrical properties of ATO films; however, limited information is available on the role of Sb and its effects on film structure [1, 24, 25]. Thus far, synthetic methods, such as pulsed laser [13, 21], sputtering [5, 8, 18], and electron-beam methods [10], carried out under vacuum conditions, have been developed to fabricate ATO thin films. However, research trends have changed from vacuum-based deposition methods to solution-based deposition approaches, such as photochemical techniques [11], sol–gel [2, 8, 12], chemical vapor deposition [9, 23], spin coating [1, 25], dip coating [4, 16, 26], and spray pyrolysis [3, 6, 7, 14, 17, 24], because of their simplicity, scalability, and low-cost device manufacturing.

Undoped and antimony-doped SnO<sub>2</sub> thin films were prepared by spray pyrolysis. The structural, electrical, and optical properties of the thin films were then examined in relationship to the increase in amount of antimony.

## 2 Experimental procedure

### 2.1 Deposition of the Sb-doped SnO<sub>2</sub> thin films by spray pyrolysis

The ATO thin films were deposited on soda lime glass substrates by spray pyrolysis. A precursor solution was prepared by dissolving 7.0116 g of 1 M SnCl<sub>4</sub>·5H<sub>2</sub>O in 20 ml of a solution containing 2-propanol and double distilled water with equal ratios. Antimony (III) chloride (SbCl<sub>3</sub>) was dissolved in the solution, with the mole concentration ratio of antimony per tin  $\frac{[Sb]}{[Sn]}$  molar ratio varying from 0 to 0.0125, 0.025, 0.05, 0.075, and 0.1 in the precursor solution, to investigate the effect of the antimony content on the physical properties of the studied samples. A few drops of hydrochloric acid was also added to the solution to enhance the solubility of tin chloride. The final solution was stirred for 30 min. Before the solution was sprayed, the substrate temperature was set at 550 °C with an accuracy of  $\pm 5$  °C by using a digital temperature controller for all of the samples. Other deposition parameters, such as spray solution volume, spray deposition rate, distance between nozzle and substrate, and hot plate rotation speed were set as follows: 20 ml, 10 ml/min, 35 cm, and 30 rpm, respectively. Before the films were prepared, the glass substrates were cleaned and placed on the hot plate. Spraying was performed in brief time intervals to prevent the rapid reduction of the hot plate temperature. The experiments were performed under similar conditions.

### 2.2 Structural, optical, and electrical characterization of films

The structural properties of the samples were examined using an X-ray diffractometer (Bruker D8 Advance) with Cu–K<sub>α</sub> radiation in the 2θ range of 20°–80°. The morphological characteristics of the films were observed using a field emission scanning electron microscope (FESEM; S-4160 Hitachi) and an atomic force microscope (AFM; 95-50-E DME). The thicknesses of the thin films were obtained on the basis of the cross-section FESEM images. An optical absorption analysis was conducted in the wavelength range of 300–1100 nm by using a double beam spectrophotometer (Unico 4802). The sheet resistance of the films and the Hall effect data were determined using the van der Pauw configuration. A temperature gradient was applied between the two ends of the samples; afterward, the thermoelectric electromotive force (EMF) of the prepared films was measured and Seebeck coefficients were determined by calculating the slope of the thermoelectric EMF versus the temperature difference. For measuring the thermoelectric electromotive force (emf) of the films, the two ends of samples were coated with aluminum by thermal evaporation in vacuum using an Edwards E-306 coating system.

## 3 Results and discussion

### 3.1 Structural characterization

Figure 1 illustrates the XRD patterns of the undoped and Sb-doped SnO<sub>2</sub> thin films. The XRD patterns reveal the

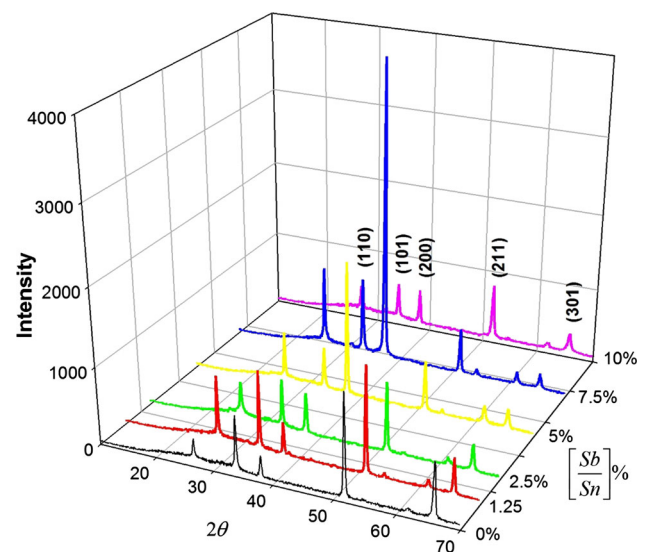


**Fig. 1** X-ray diffraction patterns of thin films

formation of the SnO<sub>2</sub> cassiterite structure. The deposited SnO<sub>2</sub>:Sb thin films are polycrystalline in nature. No Sb<sub>2</sub>O<sub>3</sub> or Sb<sub>2</sub>O<sub>5</sub> phase was detected in the XRD patterns. Antimony replaces tin in the tetragonal lattice or segregates into the non-crystalline region in the grain boundary [8]. This finding implies that the Sb ions replaced Sn ions in SnO<sub>2</sub> [1]. In Fig. 1, the undoped SnO<sub>2</sub> thin films show a preferred orientation along the (211) plane. The intensity of the preferred orientation decreased as the doping concentration increased. However, as the amount of Sb doping increased for the films doped at 1.5 to 7.5 at.%, the intensity of the (211) peak decreased and the (200) peak intensity increased. To quantitatively analyze the preferred orientation, we introduced the intensity ratio of  $\frac{I_{(200)}}{I_{(211)}}$ , where  $I_{(200)}$  and  $I_{(211)}$  are the mean peak intensities of (200) and (211) planes, respectively. As the Sb doping level increased, the intensity ratio increased: 0.27, 0.34, 0.62, 2.47, and 6.21 for the films doped with 0, 1.25, 0.5, 7.5, and 10 at.% of Sb, respectively. The peak change from (211) to (200) with increasing concentrations of Sb was also reported by Seung-Yup Lee et al. [6], E. Elangovan et al. [7] and Talaat M. Hammad et al. [27]. Secondary reflections were also observed along the planes (110), (101), (211), and (301) for thin films.

To determine the variation of crystallite size with increasing doping level, we calculated the size of the crystallites oriented along the (110), (101), (200), (211), and (301) planes by using Scherrer’s formula [28]:

$$D = \frac{k\lambda}{\delta_w \cos\theta} \tag{1}$$

where D is the average crystalline (grain) size, K is a constant (~1), λ is the X-ray wavelength, δ<sub>w</sub> is the full-width at half-maximum of XRD peaks, and θ is the Bragg angle. The calculated crystallite sizes are listed in Table 1. The average crystal size decreases as the doping level increases. This decrease is probably caused by increased

lattice distortion and inner stress induced by the Sb dopant in the matrix, and this phenomenon is called “solute drag-inhibiting grain growth” [25].

### 3.2 Morphological analysis

The FESEM images and cross-sections of undoped and Sb-doped SnO<sub>2</sub> thin films are shown in Fig. 2. The films are rough, homogeneous, compact, and adherent in nature. The surface morphological characteristics of the films were strongly dependent on the doping concentration. The layers are composed of grains with polyhedron-like shapes were distributed on the small round grains. The presence of large and faceting nanocrystals observed in these images demonstrate that the polyhedron crystallites were formed by coalescence. As the dopant concentration reached 2.5 at.% Sb doping (Fig. 2c), the average grain size increases as the doping concentration increased. In Fig. 2d, these grains became much rounder and smaller. As the Sb doping concentration further increased, the polyhedron-like grains dwindled and could hardly be distinguished from the small round grains. The average size of the large polyhedron-like grains of undoped and 1.25, 2.5, 5, 7.5, and 10 at.% Sb-doped thin films were 70, 94, 106, 108, 69, and 57 nm, respectively. The thickness of the films was estimated from the cross-sectional FESEM micrographs (Fig. 2; Table 2).

Figure 3 shows the AFM images of the thin films to help us further examine the surface morphological characteristics of the samples. The average roughness values of the undoped and 1.25, 2.5, 5, 7.5, and 10 at.% Sb-doped thin films were 45.3, 63.3, 41.1, 70.7, 72.9, and 37.3 nm, respectively. The surface morphological properties of the thin films directly affect their electrical properties. Thus, a dense surface on thin films should be obtained to improve the performance of these films. The minimum and maximum roughness values are observed at in 10 and 7.5 at.%, respectively. These values decreased the inter-grain boundary size; thus, the electrical performance of the TCOs was improved.

### 3.3 Optical analysis

The transmittance spectra as a function of the wavelength in the range of 300–1100 nm for thin films are shown in Fig. 4. The transmittances of the films decreased as the wavelength increased [6]. The average transmittance in the visible range is summarized in Table 2. The average transmittance in the visible range decreased gradually from 70 to 13 as the Sb doping concentration increased from 0 to 10 at.% [25, 29]. The decrease in transmittance is attributed to direct photon absorption and increase in photon scattering as crystal defects increased because of Sb doping. Furthermore, the free carrier absorption of photons

**Table 1** XRD results for thin films

hkl	$\frac{[Sb]}{[Sn]}$	0	1.25	2.5	5	7.5	10
(110)	D(nm)	31	30	23	32	29	25
	d(nm)	3.3415	3.4004	3.3384	3.3353	3.3366	3.3364
(101)	D(nm)	29	32	30	29	27	26
	d(nm)	2.6424	2.6418	2.6385	2.6403	2.6411	2.6411
(200)	D(nm)	27	27	25	32	28	27
	d(nm)	2.3637	2.3654	2.3610	2.3633	2.3702	2.3680
(211)	D(nm)	30	30	30	26	27	23
	d(nm)	1.7641	1.7663	1.7638	1.7653	1.7662	1.7663
(301)	D(nm)	25	30	25	25	26	19
	d(nm)	1.4162	1.4162	1.4164	1.4182	1.4194	1.4211

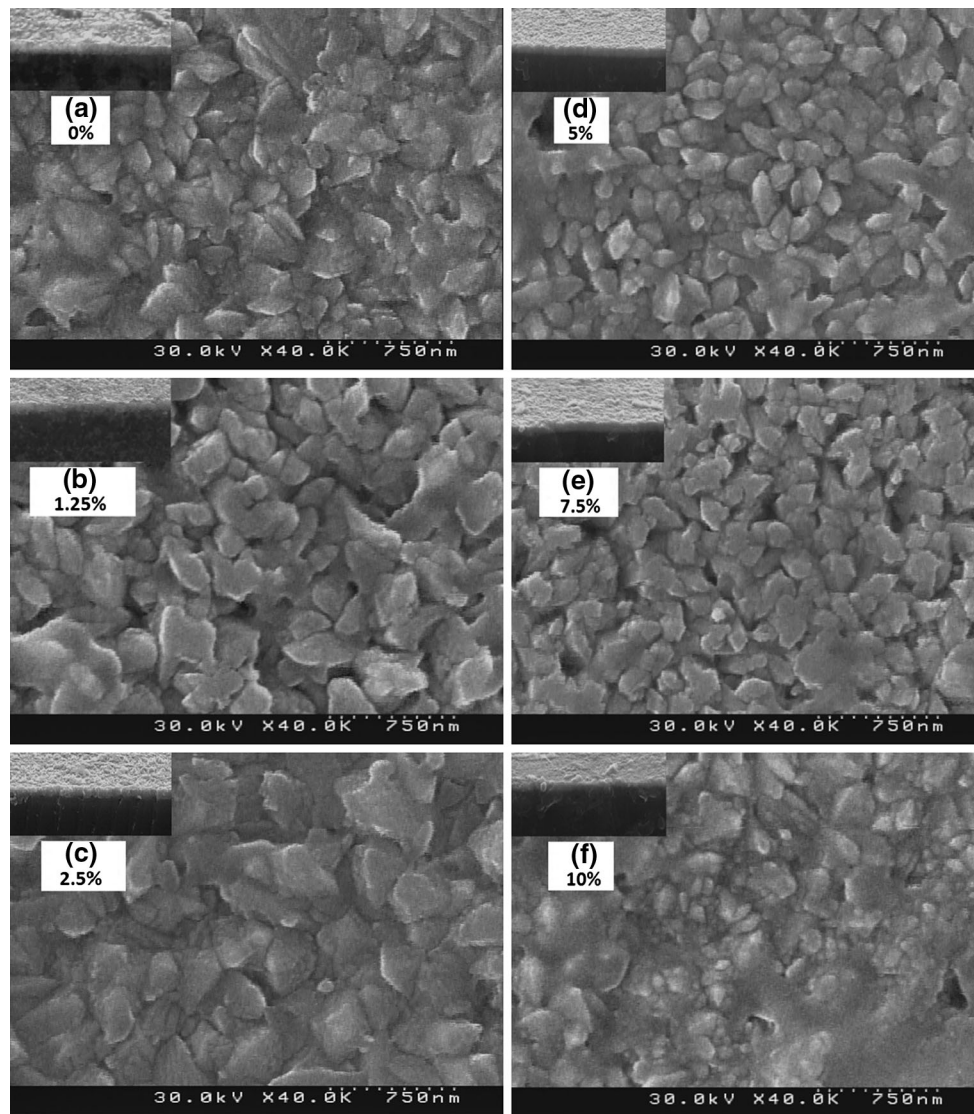


**Fig. 2** FESEM image of thin films

**Table 2** The results of optical and electrical measurements of thin films

$\left[\frac{Sb}{Sn}\right]\%$	Thickness (nm)	Average transmittance in the visible spectra	Band gap energy (eV)	Resistivity ( $\Omega$ cm)	Conductivity type	Carrier concentration $cm^{-3} \times 10^{19}$	Mobility ( $cm^2/V$ s)	Seebeck coefficient at 400 k ( $\mu V K^{-1}$ )
0	1016	70	3.5	58.5	n	3	0.35	51
1.25	1050	59	3.2	22.81	n	3.27	0.8	33
2.5	1134	67	3.8	18.31	n	3.08	0.98	31
5	983	30	3.16	16.23	n	3.72	0.62	19
7.5	1017	18	3.19	20.73	n	6.93	0.43	21
10	1033	13	3.26	44.2	n	4.09	0.33	26

may contribute to this decrease in transmittance. The crystallite size decreased significantly as the Sb doping concentration increased; thus, grain boundary scattering increased and optical transmittance decreased. The

absorption edges of the films slightly shifted to a higher wavelength as the Sb content increased. This finding is attributed to the decrease in the energy gap under the extrinsic doping effect of  $Sb^{3+}$  in  $SnO_2$ .

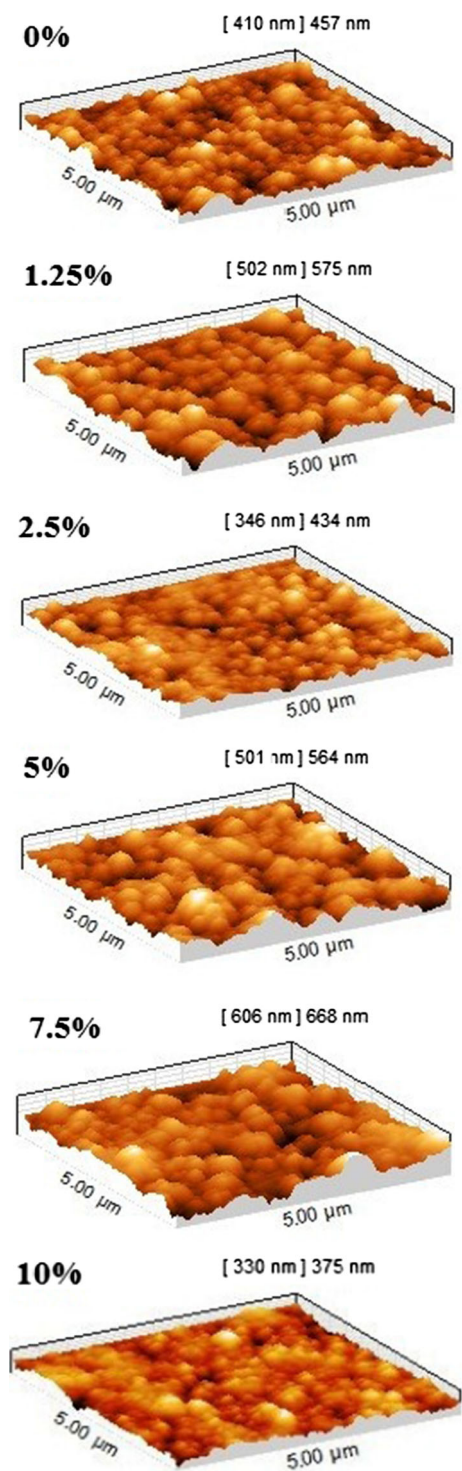


Fig. 3 AFM image of thin films

The direct optical band gap was obtained by performing optical absorption measurements and plotting  $(\alpha hv)^2$  versus photon energy ( $hv$ ) and by using Tauc's equation [28]:

$$(\alpha hv)^2 = \beta(hv - E_g) \tag{2}$$

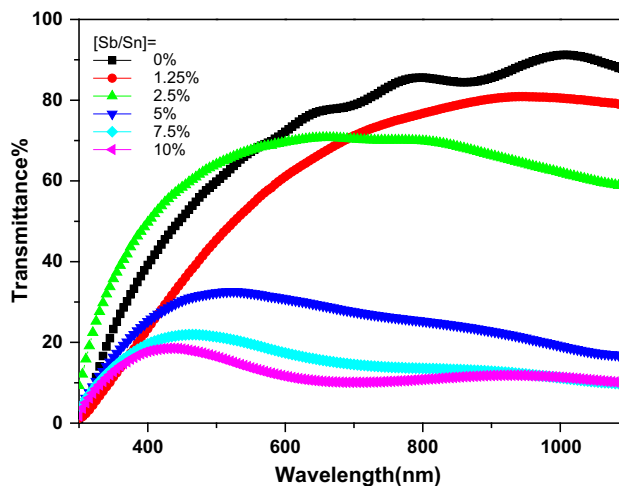


Fig. 4 The variation of transmittance versus the wavelength of thin films

where  $\alpha$  is the absorption coefficient,  $\beta$  is a constant, and  $E_g$  is the direct band gap, as shown in Fig. 5. The antimony concentration from 0 to 10 at.% decreased the optical gap  $E_g$  from 3.6 to 3.1 eV [9, 25]. The decrease in  $E_g$  could be attributed to the increase in impurity states, which may be a result of two factors. The first factor is that more states related to the  $Sb^{5+}$  impurity state are present in the ATO unit cell when more Sb atoms diffuse into the  $SnO_2$  lattice. The other factor is that the Sb dopant increased the surface state of the ATO films because of smaller crystals, as shown in the XRD results in Table 1; (Fig. 6).

### 3.4 Electrical analysis

The effect of  $\frac{[Sb]}{[Sn]}$  molar ratio on the electrical properties of the thin films was evaluated by Hall effect, resistivity

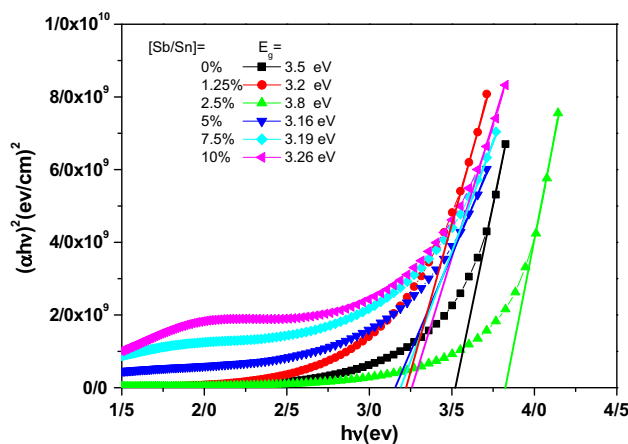
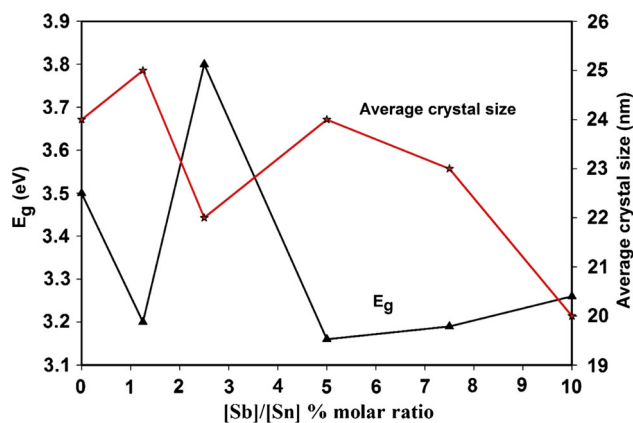


Fig. 5 Plots of  $(\alpha hv)^2$  versus  $hv$  for thin films



**Fig. 6** The variations of optical band gap  $E_g$ , and average crystal size as a function of  $\frac{[Sb]}{[Sn]}$  % molar ratio in the thin films

measurements in van der Pauw configuration, and Seebeck coefficient [30]. The room temperature variations of resistivity ( $\rho$ ), carrier density ( $n$ ), and Hall mobility ( $\mu$ ) against the  $\frac{[Sb]}{[Sn]}$  molar ratio are shown in Fig. 7, and the results are listed in Table 2. In general, the variation of the electrical resistivity of the thin films as a function of antimony doping concentration shows that resistivity decreased as antimony doping concentration increased (Fig. 7). The resistance of the undoped film is 58.5  $\Omega$  cm, but this value decreased to 16.23  $\Omega$  cm in the film with 5 at.% of antimony. The resistance increased with the doping of antimony above 5 at.%. The decreased–increased resistance of the thin films as antimony concentrations increased can be explained on the basis of the presence of Sb in two oxidation states, namely,  $Sb^{5+}$  and  $Sb^{3+}$ .

As the antimony concentration increased to 5 at.%, some of the  $Sn^{4+}$  ions in the lattice are replaced by  $Sb^{5+}$ . As a result, the conduction electrons were generated; thus, the resistance was reduced. Hence, the resistance continuously decreased until the Sb % concentration reached 5 at.%. As the concentration further increased from 5 to 10 at.%,

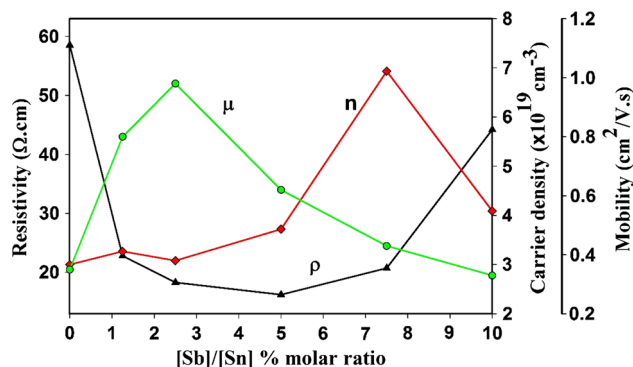


**Fig. 7** The variations of resistivity  $\rho$ , electron mobility  $\mu$ , and carrier concentration  $n$  as a function of  $\frac{[Sb]}{[Sn]}$  % molar ratio in the thin films

some of the  $Sb^{5+}$  ions are reduced to  $Sb^{3+}$ . Therefore, acceptor states were formed and carriers were concomitantly lost. Hence, the resistance increased. This trend has been observed in other studies [7, 8]. According to the FESEM results, ATO films with a small grain size exhibit poor electrical properties because of the increased scattering at the grain boundaries formed in the thin films (Fig. 8).

The carrier concentration and mobility were determined by the Hall measurement setup in van der Pauw method of the films. The Hall effect measurements confirmed that the films exhibited n-type conductivity. Figure 7 shows that the carrier concentration of the thin films increased as the Sb doping concentration increased. The carrier concentration of the undoped films was  $3 \times 10^{19}$  cm $^{-3}$  and the value increased as Sb doping concentration increased. At 10 at.% Sb doping concentration, the carrier concentration was  $4.09 \times 10^{19}$  cm $^{-3}$  [6].

The Seebeck coefficient of the thin films was measured using the steady-state method based on the EMF. With an open circuit voltage and no current flow, the Seebeck coefficients were determined in a previous study [28]:

$$s = \frac{\Delta V}{\Delta T} \quad (3)$$

where  $\Delta V$  and  $\Delta T$  are the electrical voltage and the temperature differences, respectively.

The thermoelectric properties of the thin films are shown in Figs. 9 and 10. Moreover, Seebeck coefficients at  $T = 400$  K are reported in Table 2. The variation of the thermoelectric EMF versus temperature difference of the thin films is shown in Fig. 9. The thermoelectric EMF exhibits a linear trend of temperature differences. The highest thermoelectric EMF was obtained in the undoped thin film. Figure 10 shows the variation of the Seebeck coefficient versus temperature of the thin films. The thermoelectrical effect measurements indicate the n-type conductivity of the thin films and these results were well matched with the results of Hall effect measurement. The

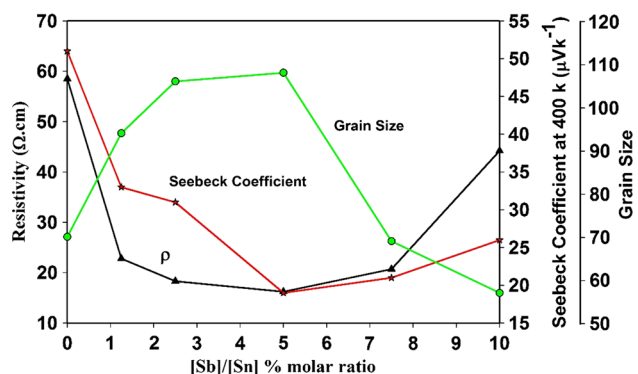


**Fig. 8** The variations of resistivity  $\rho$ , Seebeck coefficient, and grain size as a function of  $\frac{[Sb]}{[Sn]}$  % molar ratio in the thin films

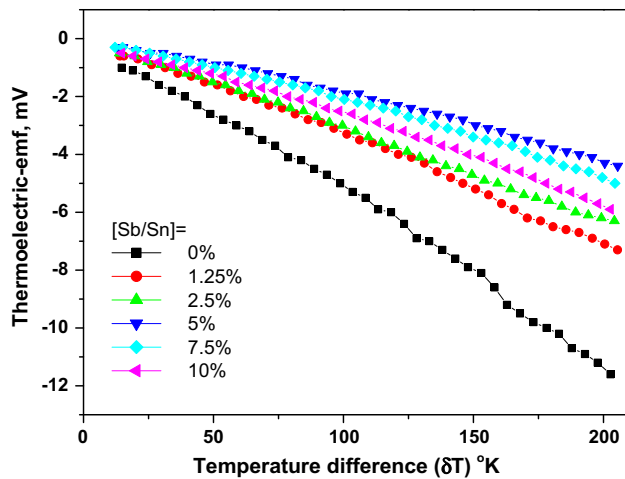


**Fig. 9** The variation of thermoelectric emf versus temperature difference of thin films

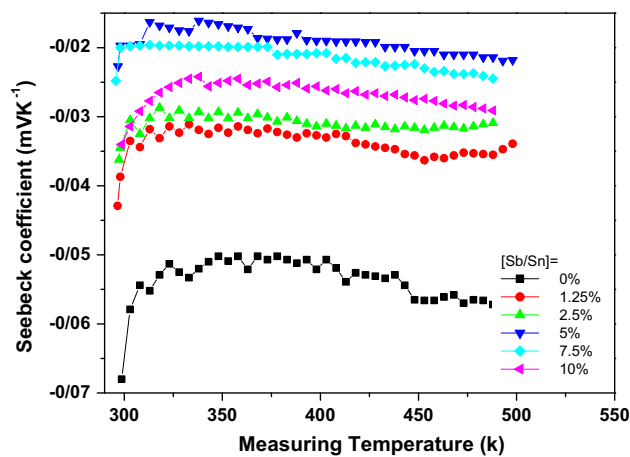


**Fig. 10** The variation of the Seebeck coefficient versus temperature of thin films

Seebeck coefficients at  $T = 400$  K showed that the decrease in Seebeck coefficient is associated with the increase in antimony concentration. However, the Seebeck coefficient of 10 at.% Sb-doped thin film is larger than those of 5 and 7.5 at.% Sb-doped thin films. This pattern of the magnitude of Seebeck coefficients may be attributed to the decrease in electrical conductivity because of the increase in grain size and the decrease in the scattering of carriers (Fig. 8).

## 4 Conclusions

In this study, undoped and antimony-doped tin dioxide thin films were prepared by spray pyrolysis. Their structural, optical, and electrical properties were determined by XRD, FESEM, AFM, UV–Vis spectroscopy, Hall effect, and Seebeck coefficient measurements. XRD results showed

that the preferred (211) orientation was observed in the undoped thin films; as the Sb doping concentration increased, the preferred (200) orientation emerged. The FESEM results showed that the thin films exhibited polyhedron-like grains, and different antimony doping levels reflected different grain sizes. The AFM analysis results revealed that roughness ranged from 37.3 to 72.9 nm. The resistivity of the  $\text{SnO}_2$  thin films was  $58.5 \Omega \text{ cm}$  and the value decreased continuously with Sb doping to  $16.23 \Omega \text{ cm}$  at 5 at.% Sb doping concentration. The carrier concentration of  $\text{SnO}_2$  thin films was  $3 \times 10^{19} \text{ cm}^{-3}$  and the value increased with Sb doping to  $6.93 \times 10^{19} \text{ cm}^{-3}$  at 7.5 at.% Sb doping concentration. The Hall mobility of  $\text{SnO}_2$  thin films was  $0.35 \text{ cm}^2/\text{V s}$ , and the value increased with Sb doping to  $0.98 \text{ cm}^2/\text{V s}$  at 2.5 at.% Sb doping concentration. The optical band gap layers ranged from 3.16 to 3.8 eV. Hall effect and thermoelectric analyses revealed that the films exhibit n-type conductivity.

**Acknowledgments** This work was supported by the Financial Support of the Research Council of Damghan University with Grant No. 93/phys/126/227.

## References

- H.-R. An, C.Y. Kim, S.-T. Oh, H.-J. Ahn, *Ceram. Int.* **40**, 385 (2014)
- B. Benrabah, A. Bouaza, A. Kadari, M.A. Maaref, *Superlattices Microstruct.* **50**, 591 (2011)
- S. Gupta, B.C. Yadav, P.K. Dwivedi, B. Das, *Mater. Res. Bull.* **48**, 3315 (2013)
- W. Mao, B. Xiong, Q. Li, Y. Zhou, C. Yin, Y. Liu, C. He, *Phys. Lett. A* **379**, 1946 (2015)
- W. Yang, S. Yu, Y. Zhang, W. Zhang, *Thin Solid Films* **542**, 285 (2013)
- S.-Y. Lee, B.-O. Park, *Thin Solid Films* **510**, 154 (2006)
- E. Elangovan, S.A. Shivashankar, K. Ramamurthi, *J. Cryst. Growth* **276**, 215 (2005)
- H.-L. Ma, X.-T. Hao, J. Ma, Y.-G. Yang, J. Huang, D.-H. Zhang, X.-G. Xu, *Appl. Surf. Sci.* **191**, 313 (2002)
- S. Haireche, A. Boumeddiene, A. Guittoum, A. El Hdiy, A. Boufelfel, *Mater. Chem. Phys.* **139**, 871 (2013)
- X. Xiao, G. Dong, J. Shao, H. He, Z. Fan, *Appl. Surf. Sci.* **256**, 1636 (2010)
- D. Ao, M. Ichimura, *J. Non Cryst. Solids* **358**, 2470 (2012)
- J. Mazloom, F.E. Ghodsi, M. Gholami, *J. Alloy. Compd.* **579**, 384 (2013)
- S. Yu, L. Ding, C. Xue, L. Chen, W.F. Zhang, *J. Non Cryst. Solids* **358**, 3137 (2012)
- B. Zhang, Y. Tian, J.X. Zhang, W. Cai, *Mater. Lett.* **65**, 1204 (2011)
- E.A. Floriano, L.V.A. Scalvi, J.R. Sambrano, A. de Andrade, *Appl. Surf. Sci.* **267**, 164 (2013)
- S.S. Lekshmy, G.P. Daniel, K. Joy, *Appl. Surf. Sci.* **274**, 95 (2013)
- R. Singh, M. Kumar, S. Shankar, R. Singh, A.K. Ghosh, O.P. Thakur, B. Das, *Mater. Sci. Semicond. Process.* **31**, 310 (2015)
- C.-M. Wang, C.-C. Huang, J.-C. Kuo, J.-L. Huang, *Surf. Coat. Technol.* **231**, 374 (2013)

19. V. Geraldo, L.V.A. Scalvi, P.N. Lisboa-Filho, C. Morilla-Santos, *J. Phys. Chem. Solids* **67**, 1410 (2006)
20. A. Novinrooz, P. Sarabadani, J. Garousi, *Iran. J. Chem. Chem. Eng.* **25**, 31 (2006)
21. S. Yu, W. Zhang, L. Li, D. Xu, H. Dong, Y. Jin, *Appl. Surf. Sci.* **286**, 417 (2013)
22. H. Zheng, L. Li, Z. Sun, S. Yu, W. Luo, *Appl. Surf. Sci.* **362**, 230 (2016)
23. Y.-Y. Lin, A.T. Wu, C.-S. Ku, H.-Y. Lee, *Jpn. J. Appl. Phys.* **51**, 10NE28 (2012)
24. B.-R. Koo, H.-J. Ahn, *Ceram. Int.* **40**, 4375 (2014)
25. S. Liu, W. Ding, Y. Gu, W. Chai, *Phys. Scr.* **85**, 065601 (2012)
26. A.A. Alsac, A. Yildiz, T. Serin, N. Serin, *J. Appl. Phys.* **113**, 063701 (2013)
27. T.M. Hammad, N.K. Hejazy, *Int. Nano Lett.* **1**, 123 (2011)
28. M.R. Fadavieslam, N. Shahtahmasebi, M. Rezaee-Roknabadi, M.M. Bagheri-Mohagheghi, *Phys. Scr.* **84**, 035705 (2011)
29. S. Shanthi, C. Subramanian, P. Ramasamy, *J. Cryst. Growth* **197**, 858 (1999)
30. L.J. van der Pauw, *Philips Res. Rep.* **13**, 1 (1958)